Hybrid Position Estimation Strategy With a Smooth Transition for IPMSM Sensorless Drives in the Wide Speed Range

Xuan Wu, Ting Wu, Shoudao Huang, *Senior Member, IEEE*, Wenli Pan, Mingcheng Lyu, Yunze He, *Member, IEEE*, and Hesong Cui

***Abstract*—In this article, an innovative hybrid position estimation strategy along with the minimum voltage vector injection (MVVI) method and the back electromotive force (back EMF) based method is proposed for interior permanent magnet synchronous motors (IPMSMs) in full-speed regions. At zero- and low-speed, the MVVI method based on rotor saliency is used for position estimation; the inverter voltage error is counteracted in estimating the rotor position, minimizing the inverter nonlinearity effect without introducing external errors. For IPMSMs at the initial state, this article proposes to utilize the high frequency *d*-axis current excited by injection voltage itself directly for the polarity detection. The position estimation at low-speed based on the MVVI method has such advantages as no requirement for filters, fast convergence, and reliability of magnetic polarity detection. In addition, a smooth transition blends the MVVI method and the back EMF based method is proposed, and a compensation term based on *q*-axis feedback current is added on the error of both the reference and feedback speed to reject the load-disturbance within the low speed and transition region. Experimental results show that the proposed hybrid sensorless control strategy exhibits excellent performance in the full speed range for both steady-state and dynamic operations.**

***Index Terms*—Hybrid position estimation, initial rotor position, interior permanent magnet synchronous motors (IPMSMS), transition.**

I. Introduction

INTERIOR permanent magnet synchronous motor (IPMSM) has been widely used in industrial applications because of its high power density, high efficiency, etc., [1]. To make use of these features, the rotor position information is essential when the field-oriented control (FOC) scheme is adopted for the IPMSM. Meanwhile, position-sensorless estimation algorithms of IPMSMs have been investigated in the last decades [2], it aims to reduce the cost and enhance the reliability of system suffering from the installation of mechanical sensors. Typically, most position estimation methods are only applicable to a range of specific speeds. In the medium- and high-speed regions, position estimation by using information found in the back electromotive force (back EMF) demonstrates a comparable performance [3]. But, the back EMF based methods fail to estimate the position at low speeds and standstill. Therefore, methods for accurate rotor-position estimation in zero- and low-speed ranges are needed to be considered. These methods in zero- and low-speed range can be roughly classified as methods based on open-loop drive [4]; modified pulsewidth modulation (PWM) methods [5]; methods based on stator current variation without additional signal [6]; and high frequency (HF) signal-injection methods [7]–[12]. To date, among methods for sensorless IPMSM drives in the full-speed region, HF signal injection methods are a proper solution in zero- and low-speed ranges. The spatial information based on machine saliencies is typically adopted for position estimation. Several saliency-based methods are reported, such as HF pulsating signal injection [7], [8], HF rotating carrier injection [9]–[10], and square-wave voltage injection [11], [12]. But the former methods need filters to extract HF current signals for position estimation and the fundamental current component for FOC [10], reducing the system bandwidth. Although the square-wave voltage injection method requires no filters [11], the inverter nonlinearities effects are not dealt with well, which is a primary issue to affect the position estimation accuracy at low-speed [12]. The compensation of the inverter voltage error can be roughly spat into two classes. Typically, the voltage error model describing the inverter characteristics or look up table [15]–[17] is established offline to compensate for the output voltage error. Compared to the square wave model, the trapezoidal wave model in [13] is more practical and effective by gradually varying the compensation voltage near the zero-current region, but this approach is perhaps less effective with transient currents, as well as the difficulty in finding a suitable threshold angle [14]. The second type of approach is to investigate new control algorithms or observers to compensate for periodic disturbances caused by voltage source inverters (VSIs), but these compensation methods may introduce new problems, such as difficulties in parameter tuning [18] or the introduction of phase delay due to the use of

Manuscript received June 27, 2021; revised November 12, 2021 and January 9, 2022; accepted February 8, 2022. Date of publication February 15, 2022; date of current version March 24, 2022. This work was supported by the Research Fund for the National Science Foundation of China under Grant 52077065. Recommended for publication by Associate Editor K. Akatsu. *(Corresponding author: Ting Wu.)*

Xuan Wu, Ting Wu, Shoudao Huang, Mingcheng Lyu, and Yunze He are with the College of Electrical and Information Engineering, Hunan University, Changsha 410006, China (e-mail: wuxuan24@163.com; wting_tata@163.com; hsd1962@hnu.edu.cn; 289763620@qq.com; hejicker@163.com).

Wenli Pan is with Zhongxing Telecom Equipment, Wuhan 430223, China (e-mail: panwl870@hnu.edu.cn).

Hesong Cui is with the Machinery Industry Beijing Electrotechnical Institute of Economic Research, Beijing 100070, China (e-mail: cuihesong@hnu.edu.cn).

Color versions of one or more figures in this article are available at https://doi.org/10.1109/TPEL.2022.3151769.

Digital Object Identifier 10.1109/TPEL.2022.3151769

filters [19]. The above methods generally need to calculate the inverter voltage error first and then compensate for it. Practically, as the digital control delay exists in most of the digital signal processor (DSP) based control systems, the pulse outputs are delayed by at least one switching period, the compensation accuracy is thus affected, even it will bring external errors. Thus, an algorithm that can minimize the inverter voltage error effects in estimating the rotor position without introducing external errors may be a good solution.

Sensorless speed-transition control from low speed to high speed also needs emphatic consideration, which mainly includes two transition methods, hysteresis transition [20]–[22], [24] and weighting transition [23], [25]–[31]. The work in [22] developed a transition scheme without parameter tuning to switch between the I–F open loop and EMF-based observer. Despite the hysteresis transition method being simple and computationally cheap, when the motor is running at the transition region, it is easy to cause speed and torque ripple at the switching point since the combined two control methods differ in the obtained position and speed at this moment [23]. Wang *et al.* [24] adopt a linear decrease of q-axis current to ensure small current and torque ripple during the transition from the I–F startup stage to the EMF-based sensorless stage, but the q-axis current decrease results in poor load-carrying performance and antidisturbance capability. Compared with the hysteresis transition method, the weighting transition method has improved in speed and torque fluctuations during the transition region to the extent, which consists of position/speed weighting transition [25]–[27] and position error weighting transition [28]–[30]. For the two position sensorless method, the position/speed weighting transition needs to blend the two-position/speed originating from the two phase-locked loop (PLL) working independently, the work in [26] presents that the HF voltage injection and sliding mode observer (SMO) based on the extended EMF are switched by position weighting transition, wherein a rotor position observer based on HF injection is designed to improve the robustness to the load disturbance. In spite of the two sets of PLL parameters that need to be designed, adjusting the parameters of both can maximize the performance of each. The position error weighting transition is based on a single PLL to switch the two position sensorless method, the position error needs to be normalized to avoid the problem of large values annihilating small values, and a smooth transition of rotor positions in the transition zone is achieved [31]. However, when the motor runs in the switching transition region and encounters a large load torque transient, the motor's operating speed changes rapidly. Due to the bandwidth limitation, PLL cannot accurately track the speed perturbation with rapid change, resulting in significant speed and position estimation errors and degradation of the dynamic performance of the sensorless control system. Therefore, the antidisturbance strategies of hybrid position estimation need to be further discussed. The work in [32] uses two Hijacker structures to act on the tracking controller and d-axis current reference, respectively, eliminating the torque ripple during the transition region to provide a smooth transition between the I–F open control and back EMF observer, but the position estimation performance at low speed is not considered.

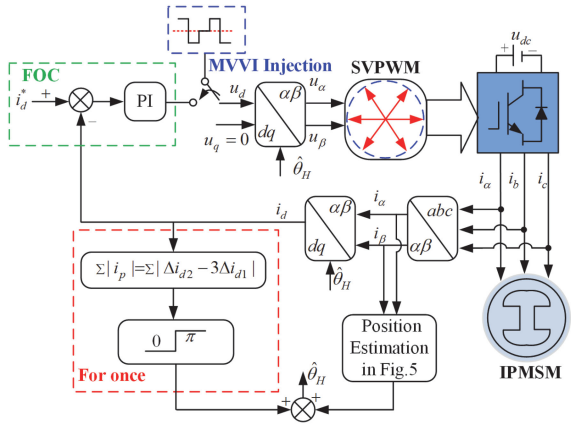

Fig. 1. Block diagram of the proposed initial position detection method.

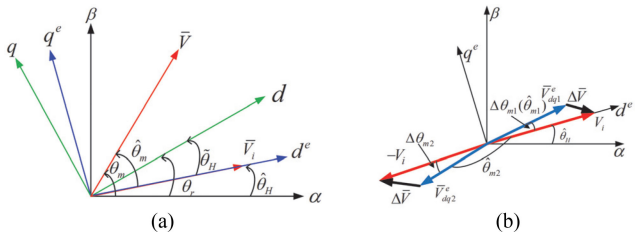

Fig. 2. Coordinate distribution of each axis. (a) One voltage vector injection scheme. (b) Two opposite voltage vectors injection scheme.

In this article, the main contribution is that a hybrid position estimation strategy for sensorless drives was proposed of covering a full-speed, capable of smooth switching and with good antidisturbance ability in the low speed and transition region. A smooth transition method blends the minimum voltage vector injection (MVVI) method and the back EMF based method is proposed. Meanwhile, a simple and effective method is proposed to reject the load-disturbance within the low speed and transition region by adding a compensation term based on q-axis feedback current on the error of both the reference and feedback speed. For the IPMSMs at the initial state, the magnet polarity is detected by judging the accumulated value of HF d-axis current variation, which is induced by the use of the same voltage injection vector. At the same time, the inverter nonlinearities effect is suppressed by injecting the positive and negative voltages separately, improving the position estimation performance at low speed. Experimental results are shown to verify the effectiveness of the proposed method implemented on a 1.5kW IPMSM drive system.

II. MVVI Method for Zero-Speed and Low-Speed Operation

This section presents an initial position estimation scheme based on the MVVI method, and its overall position estimation block diagram is shown in Fig. 1. The voltage injection period and the FOC period are separated to extract the rotor position, thus the filters are avoided. However, the saliency-based method has an ambiguity of π elec-rad when tracking the rotor position. This article proposes to utilize the HF d-axis current induced

by injection voltage itself directly for polarity detection. Thus, there is no need to inject extra signals. Next, these two parts are analyzed in detail.

A. Analysis of MVVI Method

The IPMSM voltage equations in the rotor dq-reference frame are as follows:

$$\begin{cases} v_d = Ri_d + L_d pi_d - \omega_r L_q i_q \\ v_q = Ri_q + L_q pi_q + \omega_r L_d i_d + \omega_r \lambda_{mpm} \end{cases} \tag{1}$$

where v_d, v_q, i_d, i_q are the stator d-, q-axis voltages and currents respectively; L_{d} and L_{q} are the d-, q-axis inductances; R is the stator resistance; λ_{mpm} is the peak value of the permanent magnet flux; ω_{r} is the rotor speed. $p = d/dt$ is the differential operator.

The equations in the stationary $\alpha\beta$-reference frame can be obtained from (1) as

$$\begin{aligned} \bar{v}_{\alpha\beta} = R\bar{i}_{\alpha\beta} + \left(L_{\sum} p\bar{i}_{\alpha\beta} + L_{\Delta} p\bar{i}^{*}_{\alpha\beta} e^{j2\theta_r}\right) \\ + j2\omega_r L_{\Delta} \bar{i}^{*}_{\alpha\beta} e^{j2\theta_r} + j\omega_r \lambda_{mpm} e^{j\theta_r} \end{aligned} \tag{2}$$

where $L_{\sum} = (L_d + L_q)/2$,$L_{\Delta} = (L_d - L_q)/2$, $\bar{i}^{*}_{\alpha\beta}$ is the conjugate vector of $\bar{i}_{\alpha\beta}$. When the IPMSM is at zero- and low-speed, the ω_{r} can be approximated as 0, and the last two terms (2) with respect to ω_{r} can be eliminated. At the same time, $\bar{v}_{\alpha\beta} >> R\bar{i}_{\alpha\beta}$ when the reasonable choice of injection voltage is made.

Therefore, (2) can be approximated by

$$\bar{v}_{\alpha\beta} = L_{\sum} p\bar{i}_{\alpha\beta} + L_{\Delta} p\bar{i}^{*}_{\alpha\beta} e^{j2\theta_r}. \tag{3}$$

It can be observed that

$$\bar{v}^{*}_{\alpha\beta} = L_{\sum} p\bar{i}^{*}_{\alpha\beta} + L_{\Delta} p\bar{i}_{\alpha\beta} e^{-j2\theta_r}. \tag{4}$$

The desired $p(\bar{i}_{\alpha\beta})$ can be obtained by eliminating the same $p(\bar{i}^{*}_{\alpha\beta})$, which can be expressed as

$$p\bar{i}_{\alpha\beta} = \frac{1}{L_{\Sigma}^2 - L_{\Delta}^2}(L_{\Sigma}\bar{v}_{\alpha\beta} - L_{\Delta}\bar{v}^{*}_{\alpha\beta} e^{j2\theta_r}). \tag{5}$$

Referring to Fig. 2(a), $\bar{v}_{\alpha\beta} = V_m e^{j\theta m}$, θ_m is the voltage vector angle in the $\alpha\beta$-axes. The current differentiation $p(\bar{i}_{\alpha\beta})$ can be approximated as $\Delta\bar{i}_{\alpha\beta}/T_s$ in one switching period. Therefore, (5) can be further derived as

$$\Delta\bar{i}_{\alpha\beta} = (c_1 + c_2 e^{j2(\theta_r - \theta_m)}) T_s \bar{v}_{\alpha\beta} \tag{6}$$

where $c_1 = L_{\sum}/(L_{\sum}^2 - L_{\Delta}^2)$,$c_2 = -L_{\Delta}/(L_{\sum}^2 - L_{\Delta}^2)$, T_s is the switching period.

According to Fig. 2(a), (6) can be transformed from the $\alpha\beta$-axes to the estimated dq-axes (namely the $d^e q^e$-axes), then

$$\Delta\bar{i}^{e}_{dq} = \Delta\bar{i}_{\alpha\beta} e^{-j\hat{\theta}_r} = (c_1 + c_2 e^{j2(\theta_r - \hat{\theta}_H - \hat{\theta}_m)}) T_s \bar{v}^{e}_{dq} \tag{7}$$

where $\hat{\theta}_m = \theta_m - \hat{\theta}_H$. In the FOC period, $\bar{v}^{e}_{dq} = \bar{v}_{FOC}$, $\bar{v}_{FOC}$ is the voltage vector calculated from FOC period. Note, the PI controllers of current-loop are only working in the FOC period.

In the injection period $\bar{v}_{\mathrm{FOC}} = 0$. Thus, $\bar{v}^{e}_{dq} = \bar{v}^{e}_{d} + j\bar{v}^{e}_{q} = \bar{v}_i = V_i$, where V_i is a constant voltage signal injected into the estimated d-axis.

In PWM-controlled VSIs, the dead-time, turn-ON/OFF delay, and other nonlinear switching characteristics inevitably distorted the output voltage. For motors running at low speeds, the inverter voltage errors introduced by inverter nonlinearity effects can degrade the position estimation performance. The ideal and actual switching patterns are shown in Fig. 3. The average voltage error during one switching cycle can be calculated as [33]

$$\Delta\bar{v} = \frac{T_{\mathrm{dead}} + T_{\mathrm{on}} - T_{\mathrm{off}}}{T_s}(V_{\mathrm{dc}} - V_s + V_d) + \frac{V_s + V_d}{2} \tag{8}$$

where $T_{\mathrm{dead}}, T_{\mathrm{on}}, T_{\mathrm{off}}, V_{\mathrm{dc}}, V_s$, and V_d are the dead time, turn-ON time, turn-OFF time and dc-bus voltage, switching device conduction voltage drop, and forward voltage drop of freewheeling diode, respectively. T_{dead} is the main source of the inverter voltage error.

In this article, in order to suppress the voltage error effect, one voltage vector injection scheme is further developed into injection scheme of two opposite voltage vectors. $\bar{v}_i$ can be further expressed as

$$\bar{v}_i = \begin{cases} V_i, \text{ positive half duty} \\ -V_i, \text{ negative half duty.} \end{cases} \tag{9}$$

Fig. 4 shows the sequence of the proposed MVVI method. The currents are sampled at the beginning of the PWM carrier period. After updating the output voltage during the FOC period,

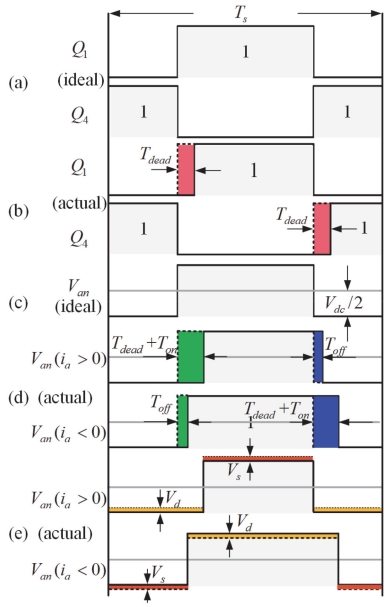

Fig. 3. Switching mode and output pole voltage. (a) Ideal upper and lower IGBT gate signals. (b) Actual gate signal. (c) Ideal output pole voltage. (d) Actual output pole voltage considering dead-time and turn-ON/OFF time. (e) Actual output pole voltage considering voltage drop.

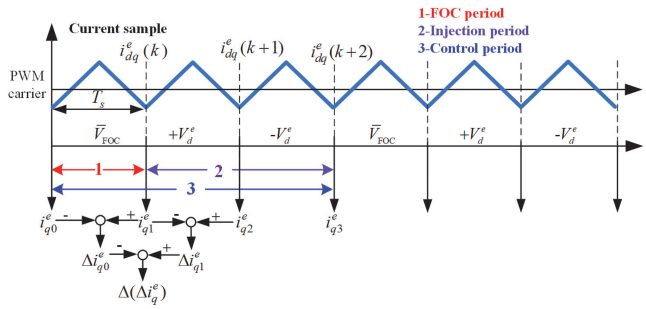

Fig. 4. Implementation sequence of the MVVI method.

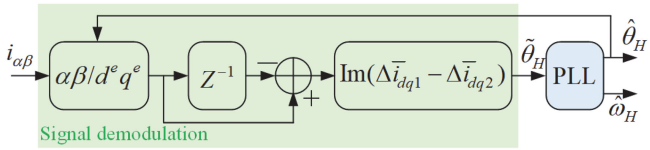

Fig. 5. Rotor position information extraction based on MVVI method.

two positive and negative voltage vectors are injected on the estimated d-axis sequentially. The sampled q-axis current between an injection period makes a difference to obtain $\Delta i^e_{q0}$and Δi^e_{q1} , then the difference $\Delta(\Delta i^e_{q1})$made by the adjacent q-axis currents variation can be utilized to estimate the rotor position. During execution, the injection period is separated from the FOC period, and the measured current variation during the injection period can be used directly for position estimation.

The position estimation errors are compensated by injecting two opposite voltage signals (V_i and -V_i) on the estimated d-axis. Assuming that the voltage error $\Delta\bar{V}$caused by inverter nonlinearities effects will be the same in two injection switching periods, the real voltage provided to the IPMSM can be written as

$$\bar{V}^e_{dq1} \approx V_i - \Delta\bar{V} \tag{10}$$

$$\bar{v}^e_{dq2} \approx -V_i - \Delta\bar{v} \tag{11}$$

where subscripts 1 and 2 mean the first half injection period and the second half injection period, respectively.

According to (10) and (11), the resultant current variations of (7) can be further derived as

$$\Delta\bar{i}^e_{dq1} = (c_1 + c_2 e^{j2(\theta_r - \hat{\theta}_H - \hat{\theta}_{m1})}) \cdot (V_i - \Delta\bar{v})T_s \tag{12}$$

$$\Delta\bar{i}^e_{dq2} = (c_1 + c_2 e^{j2(\theta_r - \hat{\theta}_H - \hat{\theta}_{m2})}) \cdot (-V_i - \Delta\bar{v})T_s \tag{13}$$

where $\hat{\theta}_{m1}$ and $\hat{\theta}_{m2}$ is the phase difference that $\bar{v}^e_{dq1}$ and $\bar{v}^e_{dq2}$ deviated from the estimated d-axis, respectively.

As it is observed from Fig. 2(b), $\hat{\theta}_{m1} = \Delta\theta_{m1}$,$\hat{\theta}_{m2} = \pi - \Delta\theta_{m2}$, and $\Delta\theta_{m1} \approx \Delta\theta_{m2}$. It is not difficult to find that

$$\Delta\bar{i}^e_{dq1} - \Delta\bar{i}^e_{dq2} = 2c_1T_sV_i + 2c_2e^{j2(\tilde{\theta}_H - \Delta\theta_{m1})}V_iT_s. \tag{14}$$

It is noted that the angle $\Delta\theta_{m1}$ is very close to zero, (14) can be simplified as

$$i_{posi} = \mathrm{Im}(\Delta\bar{i}^e_{dq1} - \Delta\bar{i}^e_{dq2}) = 2k_\varepsilon \sin(2\tilde{\theta}_H) \approx 4k_\varepsilon\tilde{\theta}_H \tag{15}$$

where $k_\varepsilon = c_2T_sV_i$ is a constant.

From (15), the voltage error$\Delta\bar{v}$ has been counteracted, which means that the inverter nonlinear error has been eliminated effectively. The position information also has been contained in the terms of i_{posi}.The estimated rotor position $\hat{\theta}_H$ and speed $\hat{\omega}_H$ can be extracted by applying a normalized PLL, as shown in Fig. 5.

B. Proposed Magnetic Polarity Identification Method

Note that when i_{posi} is changed to zero, $\tilde{\theta}_H$ can be either 0 or 180 electrical deg. Therefore, the magnetic polarity detection process is necessary.

The magnetic polarity information can be obtained from the real part of (14) as

$$i_{\mathrm{pola}} = \mathrm{Re}(\Delta\bar{i}^e_{dq1} - \Delta\bar{i}^e_{dq2})$$

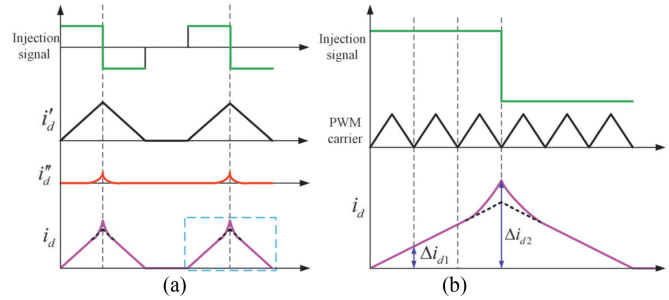

Fig. 6. d-axis current induced by injection when the IPMSM is at N-pole. (a) When the injection period equals two PWM periods. (b) When the injection period equals six PWM periods.

$$= 2c_1T_sV_i + 2c_2T_sV_i\cos 2(\tilde{\theta}_H - \Delta\theta_{m1}). \tag{16}$$

According to (6), the coefficient c_1 is much larger thanc_2. Therefore, the term $2c_1T_sV_i$ is dominant in the i_{pola}.Then, (16) can be simplified as

$$i_{\mathrm{pola}} = 2T_sV_i/L_\Sigma. \tag{17}$$

In (17), the magnitude of i_{pola} is inversely proportional to the average inductance, L_Σ , with the voltage vector V_i and -V_i injected respectively in the d^e-axis and minus d^e-axis. $L_\Sigma$has different value at different saturation conditions. Therefore, the induced current variation of d-axis can be used for magnetic polarity detection.

Fig. 6 shows the induced d-axis current when the rotor is at the direction of N-Pole. In Fig. 6(a), i'_drepresents the current value without the saturation. The amplitude of the i''_d depends on i_d, indicating the saturation degree. The magnetic saturation effect is magnified by two opposite injection voltage. It further drives $L_\Sigma$into decreasing, then the current i_d induced by injection signal is enhanced, and the peak value of i_d is slightly larger than i'_d. On the contrary, when the rotor position is S-pole, i_d keeps its normal value asi'_d.

Note, the switching periodT_s and injection period T_i have a proportional relationship as

$$T_i/T_s = k_n, k_n \geq 1 \tag{18}$$

where k_n is a constant.

For the selection of k_n , it includes the following two cases.

1) $k_n = 6$. When the motor is at the initial state, in order to make full use of the magnetic saturation effect for magnetic polarity detection, the value of k_n is usually greater than 1, so that the stator core is fully saturated.
2) $k_n = 2$. When the initial position detection is completed and the motor starts running, the smaller the value of k_n, the higher the frequency of rotor position estimation update and the faster the dynamic response of system. k_n may even be equal to 1 in the double-sampling, and dual-update mode.

The injection period equals six PWM periods illustrated in Fig. 6(b). Δi_{d2} is larger than $3\Delta i_{d1}$ when the rotor position is at N-pole. In contrast to S-pole, Δi_{d2} is equal to $3\Delta i_{d1}$. Despite this criterion can theoretically be used for magnetic polarity detection, due to the very short injection period, the response current amplitude is small. That is to say, the current difference

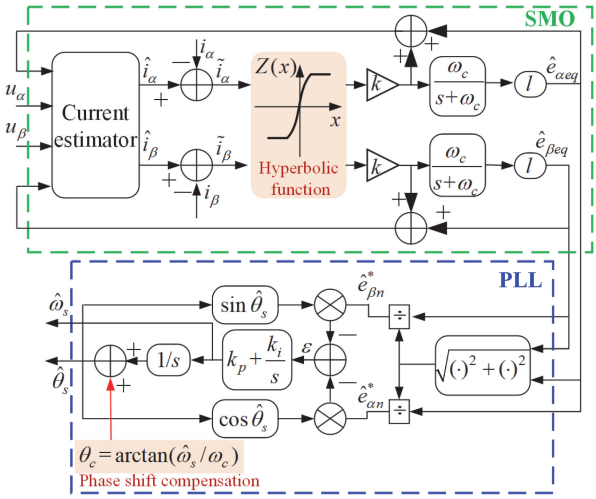

Fig. 7. Block diagram of position estimation based on SMO.

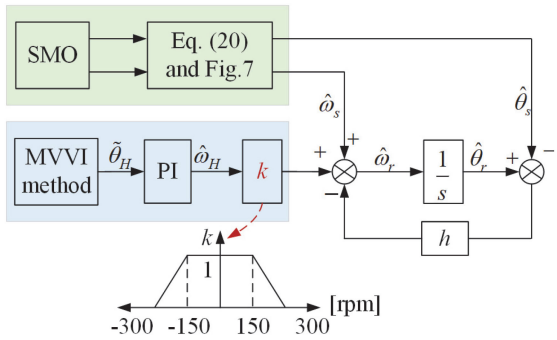

Fig. 8. Block diagram of transition algorithm.

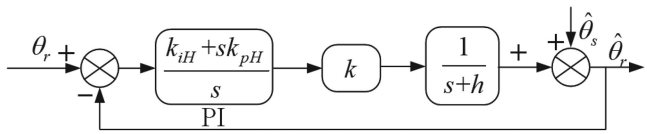

Fig. 9. Equivalent scheme of the transition algorithm structure in Fig. 8.

$i_p = \Delta i_{d2}$-$3\Delta i_{d1}$ is small, and other noise may interfere with the detection results. Thus, the accumulation form of $i_p = \Delta i_{d2}$-$3\Delta i_{d1}$ in a certain period is considered. If the rotor position is at N-pole, a positive number $\Sigma|i_p|$ should be produced. Contrarily, if the rotor position is at S-pole, the $\Sigma|i_p|$ will be approximately zero. In this article, a cumulative time of 10ms about $\Sigma|i_p|$ is considered.

III. Back EMF Method for Middle- and High-Speed Operation

Beyond the zero and low-speed range, the back EMF signal is sufficiently reliable that it can be used to detect the rotor position. SMO for position estimation has the advantages of parameter insensitivity, robustness, etc. It will be adopted to obtain the rotor position at the middle and high speed.

A dynamic sliding mode motion equation can be represented as

$$\begin{bmatrix} p\tilde{i}_\alpha \\ p\tilde{i}_\beta \end{bmatrix} = A\begin{bmatrix} \tilde{i}_\alpha \\ \tilde{i}_\beta \end{bmatrix} - \frac{1}{L_d}\begin{bmatrix} l\hat{e}_{\alpha eq} + Z(\tilde{i}_\alpha) - e_\alpha \\ l\hat{e}_{\beta eq} + Z(\tilde{i}_\beta) - e_\beta \end{bmatrix}$$
$$A = \frac{1}{L_d}\begin{bmatrix} -R & -\hat{\omega}_s(L_d - L_q) \\ \hat{\omega}_s(L_d - L_q) & -R \end{bmatrix} \tag{19}$$

where $\tilde{i}_\alpha = \hat{i}_\alpha - i_\alpha$ and $\tilde{i}_\beta = \hat{i}_\beta - i_\beta$, $\hat{i}_\alpha$ and $\hat{i}_\beta$ are observed currents. $\hat{\omega}_s$is the estimated speed. e_α and e_β are the $\alpha\beta$-axes back EMF. $Z(x) = k\tanh(\lambda x)$ is the hyperbolic tangent saturation function, effectively weakening the system chattering to a certain extent. λ is a positive constant used to regulate the boundary layer of hyperbolic function [34]. k is the sliding mode gain, which can be derived to meet the criteria to ensure the stability of the designed SMO, as seen in the Appendix. The equivalent control $\hat{e}_{\alpha\beta eq}$ can be obtained by applying a low-pass filter (LPF) to $Z(x)$, which extends the operating speed of SMO and improves the position estimation performance [35]. $l$is the feedback gain of the equivalent control $\hat{e}_{\alpha\beta\mathrm{eq}}$.

To compensate for the delay introduced by the LPF, an additional compensation term θ_c is added to the calculated position to obtain the final position, as shown in Fig. 7, ω_c is the cut-off frequency of the LPF. The estimated rotor position can be written as

$$\hat{\theta}_s = \frac{1}{s}\left(\frac{k_i}{s} + k_p\right)\frac{1}{\sqrt{\hat{e}_{\alpha\mathrm{eq}}^2 + \hat{e}_{\beta\mathrm{eq}}^2}}(-\hat{e}_{\alpha\mathrm{eq}}\cos\hat{\theta}_s - \hat{e}_{\beta\mathrm{eq}}\sin\hat{\theta}_s) \tag{20}$$

where k_i and k_p are the control parameters of the PLL.

IV. Transition Algorithm and Anti-disturbance Strategy

It is noted that the proposed MVVI method based on saliency is suitable for zero- and low-speed. As the machine speed increases, the saliency-based method needs to be switched to the SMO based on back EMF. For the reason that the magnitude of back EMF voltage is enhanced with speed, then the dc-bus voltage is not enough for the voltage injection. Thus, a transition algorithm is necessary for the full-speed drive to be switched smoothly and rapidly.

A. Transition Algorithm

Fig. 8 depicts the proposed hybrid position observer combining the SMO method with the MVVI method. The gain k is intercalated to turn the MVVI method loop on and off. The transition in this article operates between 5% and 10% rated speed. When the motor is running below 150 r/min, the value of k is equal to 1. Namely, only the MVVI method works in position estimation. When the motor is running between 150 and 300 r/min, the value of k scales down from 1 to 0. However, when the speed is above 300 r/min, the MVVI method along with the PI output is removed completely, and then the SMO method starts to be implemented.

For the convenience of analysis, the transition structure in Fig. 8 is taken as the scheme shown in Fig. 9. The estimated

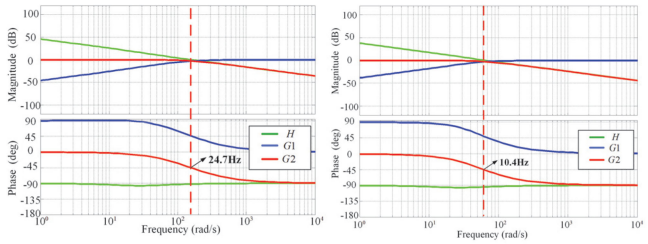

(a) (b)

Fig. 10. Bode diagram of (21). (a) When $k = 1$ (within 150 r/min). (b) When $k = 0.4$ (240 r/min).

position$\hat{\theta}_r$ can be derived as

$$\begin{cases} \hat{\theta}_r = G_1 \cdot \hat{\theta}_s + G_2 \cdot \theta_r \\ G_1 = \frac{1}{1+H} \\ G_2 = \frac{H}{1+H} \\ H = \frac{k_{iH}+s\cdot k_{pH}}{s} \cdot k \cdot \frac{1}{s+h}. \end{cases} \tag{21}$$

In (21), the G_2 and G_1 are the transfer functions of the MVVI method and the SMO method, respectively. H is the open-loop transfer function of the MVVI method tracking loop.When the speed is less than 150 r/min, the Bode diagram of G_2 and G_1 in (21) is shown in Fig. 10(a). The $\tilde{\theta}_H$ with normalization entered the PI controller, and $k_{pH} = 160$, $k_{iH} = 5000$. The gain h sets as 25 rad/s. As shown in Fig. 10, the bandwidth of transfer function G_2 based on the MVVI method is about 24.7 Hz in the steady-state. Although the MVVI method is switched on, the position information obtained from the SMO is always available.

If rotor speed increases from 150 to 300 r/min, the value of k decreases from 1 to 0 in a certain proportion. The open-loop characteristic (H) also moves down, leading to the cutoff frequency based on the MVVI method to lower frequencies. The Bode diagrams with $k = 0.4$ are as shown in Fig. 10(b). The bandwidth of position estimation based on the MVVI method is approximately 10.4 Hz. It means that position estimation based on SMO will be active at lower frequencies, while the bandwidth of position estimation based on the MVVI method loop decreases gradually. Therefore, the bandwidth has been greatly expanded. When the speed goes beyond 300 r/min where $k = 0$, the observed angle is only from the SMO ($\hat{\theta}_r = \hat{\theta}_s$), and the MVVI method is abandoned completely.

B. Impact of Load Sudden Change on Transition Method

The transition blends the two positions and speeds from the two PLL, the performance of PLL affects the transition performance inevitably. When the machine encounters a sudden load change, the motor's operating speed can change rapidly, often exceeding the bandwidth of the PLL. In this case, the PLL is unable to accurately track the speed disturbance with rapid variation, resulting in remarkable speed and position estimation errors.

The small-signal analysis can be given to illustrate the effects of load sudden change on the speed estimation error. The mechanical equation of IPMSM is expressed as

$$T_e - T_L = \frac{J}{n_p} p\omega_r + B\frac{\omega_r}{n_p} \tag{22}$$

where T_e is the electromagnetic torque, T_L is the load torque, B is the viscous friction coefficient, and J is the moment of inertia, n_p is pole pairs.

When the motor operates at a steady-state, the differential of the speed is zero, and (22) can be derived as

$$T_{e0} - T_{L0} - B\frac{\omega_{r0}}{n_p} = 0. \tag{23}$$

When a load torque disturbance is imposed on the machine, the variables in (22) will be around the steady state value produce a certain increment, as expressed as

$$\begin{cases} T_e = T_{e0} + \Delta T_e \\ T_L = T_{L0} + \Delta T_L \\ \omega_r = \omega_{r0} + \Delta\omega_r \\ p\omega_r = 0 + p\Delta\omega_r \end{cases} \tag{24}$$

where the symbol Δ indicates the small increment generated by a small disturbance to the motor.

Substitute (24) into (22) and subtract (23), the perturbation dynamic equation can be expressed as follows:

$$\Delta T_e - \Delta T_L - \frac{B}{n_p}\Delta\omega_r = \frac{J}{n_p} p\Delta\omega_r. \tag{25}$$

As can be seen from (25), the electromagnetic torque ΔT_e always tries to cancel the load torque disturbance ΔT_L to bring the system back to steady-state. But, ΔT_e will inevitably lag behind ΔT_L due to the limitation of system performance. Hence, the relationship between ΔT_e and ΔT_L can be described as follows:

$$\Delta T_e = \frac{1}{\tau s+1}\Delta T_L. \tag{26}$$

Substitute (26) into (25) and transformed as frequency domain, as derived as

$$\Delta\omega_r = -\frac{\tau s}{\tau s+1} \cdot \frac{n_p}{B+Js} \cdot \Delta T_L. \tag{27}$$

It is clear from (27) that the perturbation of the load torque will cause a fluctuation in the rotor speed. Although the transient performance of PLL can be improved by selecting a large bandwidth, it will bring noise to the estimated speed, a tradeoff has to be made to take into account when designing the parameters of PLL. Hence, the anti-disturbance strategy needs to be considered to improve the dynamic performance in the transition region.

C. Disturbance Compensation

The simplified speed-loop diagram based on hybrid position estimation is illustrated in Fig. 11, wherein the transfer function of hybrid position observer is expressed as

$$G_o = \frac{\hat{\omega}_r}{\omega_r} = \frac{k \cdot k_{pH} s + k \cdot k_{iH}}{s^2 + (h+k_{pH})s + k \cdot k_{iH}}. \tag{28}$$

In order to evaluate the antidisturbance of the system, the stiffness is introduced in this article, which is a useful indicator of robustness, and defined as the interference required to produce a unit error in the output [36]. In this article, the stiffness refers to the drive's closed-loop stiffness, i.e., the torque disturbance

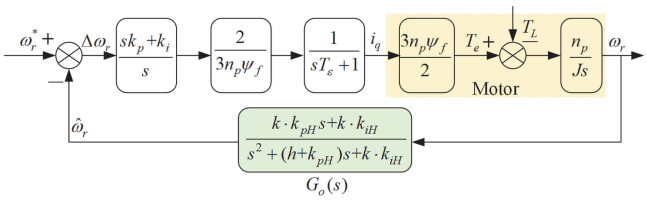

Fig. 11. Simplified diagram of the speed loop based on proposed hybrid position estimation method without disturbance compensation.

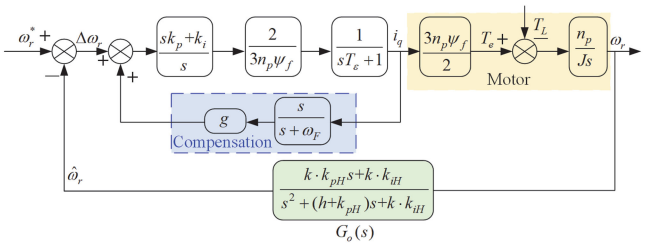

Fig. 12. Modified speed loop based on proposed hybrid position estimation method with disturbance compensation.

required to generate a per-unit error in speed ($T_L/\hat{\omega}_r$) when using closed-loop speed control with hybrid position estimation. The close loop transfer function of load torque related to the estimated speed as per Fig. 11 can be derived as

$$\frac{\hat{\omega}_r}{T_L} = \frac{n_0 s^5 + n_1 s^4 + n_2 s^3 + n_3 s^2}{m_0 s^5 + m_1 s^4 + m_2 s^3 + m_3 s^2 + m_4 s + m_5 k_i} \tag{29}$$

where (30) shown at the bottom of this page,

From the analysis of (27), the system stiffness is reduced due to deviations between the observed and actual rotor position and speed, especially in the case of sudden load change. A simple and effective method is proposed to reject the load disturbance within the low speed and transition region by adding a compensation term based on q-axis feedback current on the error of both the reference and feedback speed. The compensation term can be expressed as

$$\omega_{\text{com}} = \frac{s}{s + \omega_F} \cdot g \cdot i_q \tag{31}$$

where g and ω_F are the compensation gain and the filter cutoff angular frequency, respectively.

The modified speed loop based on hybrid position estimation as per (31) is illustrated in Fig. 12, and the modified close loop transfer function of (29) can be derived as, (32) shown at the bottom of this page, where, (33) shown at the bottom of the next page.

TABLE I
PARAMETERS OF THE IPMSM

Parameters	Values
Rated Power /kW	1.5
Rated voltage /V	380
Rated current /A	2.7
Rated speed /(r/min)	3000
Number of pole pairs	2
d-axis inductance/mH	17.81
q-axis inductance/mH	26.72
Stator Resistance/Ω	2.2

The amplitude–frequency response characteristics of stiffness are shown in Fig. 13. Different compensation gain and cutoff frequency are given in Fig. 13(a) and (b), respectively. As can be seen in Fig. 13(a), the magnitude of stiffness goes up with the compensation gain g increases in the low frequency domain, which indicates the load disturbance rejection capability of the system increases accordingly. Moreover, the lower the disturbance frequency, the stronger the stiffness of the system compared to the case of $g = 0$ (without compensation). On the other hand, when the compensation gain g is set as 2, the disturbance rejection ability is greater for lower values of the cutoff frequency ω_F, but the relatively small change in amplitude. Thus, the compensation term is to be selected with low values of the cutoff frequency to obtain the highest damping capability.

V. EXPERIMENTAL RESULTS

The experiment has been performed to test the effectiveness of the proposed method. The system setup for experimental is illustrated in Fig. 14. The parameters of IPMSM drive are given in Table. I. In the experiment, TMS320F2808 DSP is adopted to execute the full-speed sensorless position estimation algorithm. An induction motor is mechanically coupled to the IPMSM. The actual rotor position and speed are measured by incremental encoder PENON-K3808G, these obtained results are used to compare with the estimated and not involved in a closed-loop position estimation system.

The position estimation of the MVVI method depends on the detection of the current variation caused by the injected voltage. An appropriate increase in the injection period can give more time for the current to vary, which leads to a larger current variation and better position estimation performance. If the injection period is too long, the estimated rotor position is updated slowly because it will not be updated during the control period until the next voltage vector is injected to provide a new

$$\begin{cases} \text{A} = k \cdot k_{pH}, B = k \cdot k_{iH}, C = h + k_{pH} \\ n_0 = JT_\varepsilon; n_1 = J; n_2 = JCT_\varepsilon; n_3 = JC; n_4 = JBT_\varepsilon; n_5 = JB \\ m_0 = JT_\varepsilon; m_1 = J + JCT_\varepsilon; m_2 = JC + JBT_\varepsilon; m_3 = JB + n_p A k_p \\ m_4 = Bn_p k_p + n_p A k_i; m_5 = Bn_p k_i \end{cases} \tag{30}$$

$$\frac{\hat{\omega}_r}{T_L} = \frac{-n_p}{J} \cdot \frac{\text{b}_0 s^7 + b_1 s^6 + b_2 s^5 + b_3 s^4 + b_4 s^3 + b_5 s^2}{a_0 s^9 + a_1 s^8 + a_2 s^7 + a_3 s^6 + a_4 s^5 + a_5 s^4 + a_6 s^3 + a_7 s^2 + a_8 s} \tag{32}$$

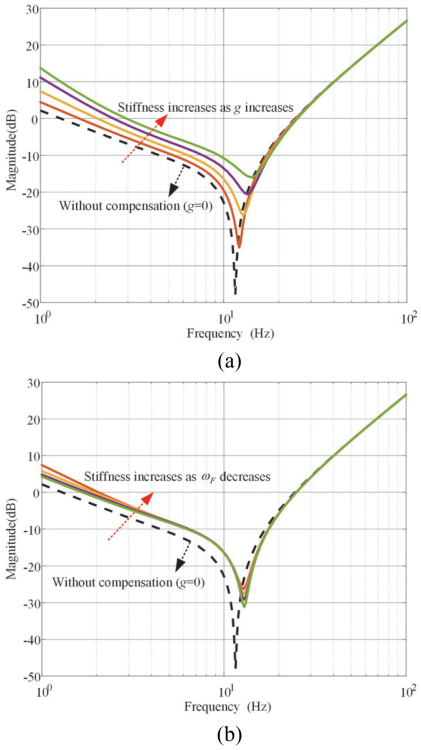

Fig. 13. Bode magnitude plots of the stiffness. (a) g increases from 1 to 4 and $\omega_{\mathrm{F}} = 12.6$ rad/s. (b) ω_{F} increases from 12.6 rad/s to 31.4 rad/s and $g = 2$.

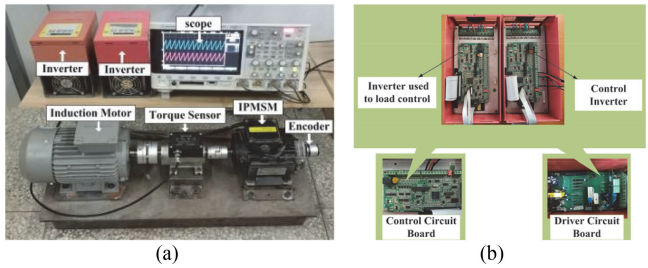

Fig. 14. Experimental platform. (a) Whole experimental test. (b) Inverter for control platform.

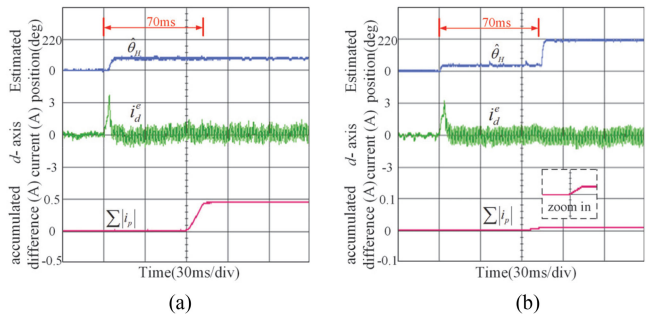

Fig. 15. Initial rotor position estimation when the motor is operated at standstill. (a) When the rotor position is initially locked at 100°. (b) When the rotor position is initially locked at 220°.

position estimate, which will lead to position estimation errors or even make the FOC unstable. On the other hand, if the injected period is too short, the system will suffer from audible noise and switching loss. Consequently, in order to obtain good position estimation performance at low-speed (nonzero), it is recommended to choose a range of FOC periods, injection period, and control period is 0.1–0.4 ms, 0.2–0.8 ms, and 0.3–1.2 ms, respectively. The sampling frequency is the same as the PWM switching frequency adopted with 5 kHz in this article. The control period is 0.6 ms, the injection period (0.4 ms) is twice the FOC period (0.2 ms) when the motor rotates at low speed (nonzero) with the MVVI method. The voltage injection amplitude of the MVVI method is set as 90 V. $k = 50000$, $\lambda = 0.01$, and $l = -0.5$ when the rotor speed is below 300 r/min, otherwise, $l = 1$.

A. *Standstill and Low-Speed Startup Operation of IPMSM*

Fig. 15 shows the experimental waveforms of initial position detection based on the MVVI method. The injection period of MVVI method is 1.2 ms. The whole position estimation process is performed in 70 ms.

In Fig. 15(a), the rotor position was initially located at $\theta_r = 100°$. When the estimated position was converged, the estimated initial position $\hat{\theta}_H$ was obtained as 102.4°. At the same time, the cumulative value of the current difference i_p was obtained. It can be found that $\Sigma|i_p|$ is greater than 0. Therefore, $\hat{\theta}_H$ is not to be corrected. Finally, the estimated rotor position $\hat{\theta}_H$ is 102.4°, and the position estimation error is 2.4°. Fig. 15(b) shows that the motor is operated in a standstill situation when the rotor position is initially located at $\theta_r = 220°$. Once the estimated position is converged, the estimated initial position $\hat{\theta}_H$ is obtained as 41.3°. At the same time, the result is $\Sigma|i_p| \approx 0$. Thus, an electrical

$$
\begin{cases}
k_t = 3n_p\psi_f; L_0 = n_p k_p A, L_1 = n_p(A(k_i + \omega_F k_p) + Bk_p) \\
L_2 = n_p(A\omega_F k_i + B(k_i + \omega_F k_p)), L_3 = n_p B\omega_F k_i \\
M_0 = Jk_t T_\varepsilon, M_1 = J(k_t T_\varepsilon C + k_t T_\varepsilon \omega_F + 2gk_p + k_t) \\
M_2 = J(k_t T_\varepsilon B + (k_t T_\varepsilon \omega_F + 2gk_p + k_t)C + k_t\omega_F + 2gk_i) \\
M_3 = J(B(k_t T_\varepsilon \omega_F + 2gk_p + k_t) + (k_t\omega_F + 2gk_i)C), \\
M_4 = J(k_t\omega_F + 2gk_i)B \\
b_0 = AM_0, b_1 = AM_1 + BM_0, b_2 = AM_2 + BM_1, b_3 = AM_3 + BM_2 \\
b_4 = AM_4 + BM_3, b_5 = BM_4 \\
a_0 = M_0, a_1 = CM_1 + M_0, a_2 = M_0 B + CM_1 + M_2 \\
a_3 = BM_1 + CM_2 + L_0 + M_3 \\
a_4 = BM_2 + C(L_0 + M_3) + L_1 + M_4, a_5 = B(L_0 + M_3) + C(L_1 + M_4) + L_2 \\
a_6 = B(L_1 + M_4) + CL_2 + L_3, a_7 = BL_2 + L_3 C, a_8 = L_3
\end{cases}
\tag{33}
$$

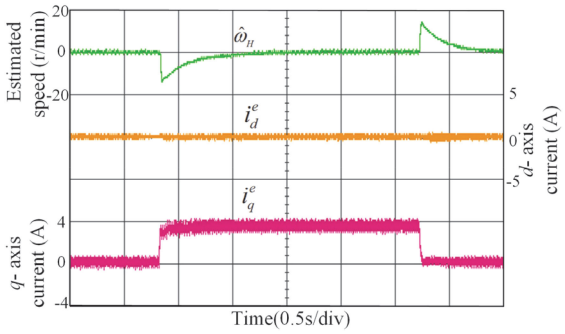

Fig. 16. Position estimation performance at standstill with load step.

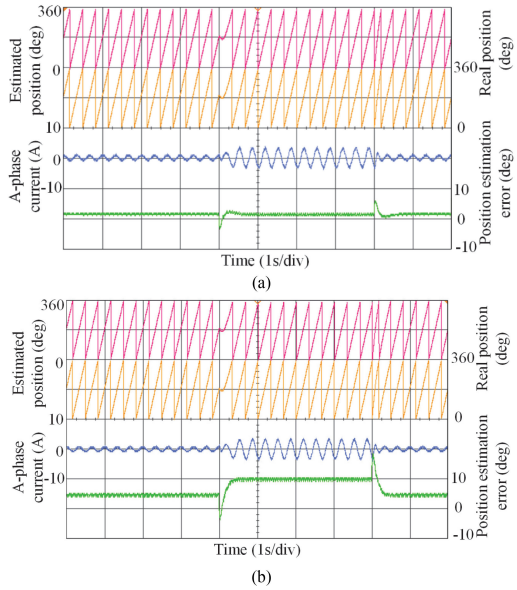

Fig. 17. Comparison of position estimation performance under step load disturbance. (a) With compensation. (b) Without compensation.

angle of 180° should be added on $\hat{\theta}_H$. Finally, the estimated rotor position $\hat{\theta}_H$ is 221.3°, and the position estimation error is 1.3°. It is worth noting that the value of $|i_p|$ was not completely zero. The accumulated term is the absolute value of i_p, so the accumulated result is a very small positive value.

Fig. 16 shows the experimental waveform of estimated speed, and current change when the motor was suddenly loaded and unloaded in the standstill situation. When the motor is at standstill, with a sudden increase in rated load and sudden removal of the rated load, the motor had a temporary speed fluctuation, and then quickly returned to a stable value. The speed transient error was not exceeded 15 r/min. A satisfactory stability and fast dynamic response are obtained.

The comparison of inverter nonlinearity compensation between one voltage injection and two opposite voltage injection based on MVVI method is illustrated in Figs. 17 and 18. In Fig. 17, when the machine operated stably at 90 r/min with 30% rated load, the position estimation error was 2° in Fig. 17(a), and it becomes 5° without the inverter voltage error compensation in Fig. 17(b), it reflects that the two opposite voltage injection strategy has better steady-state performance compared with the

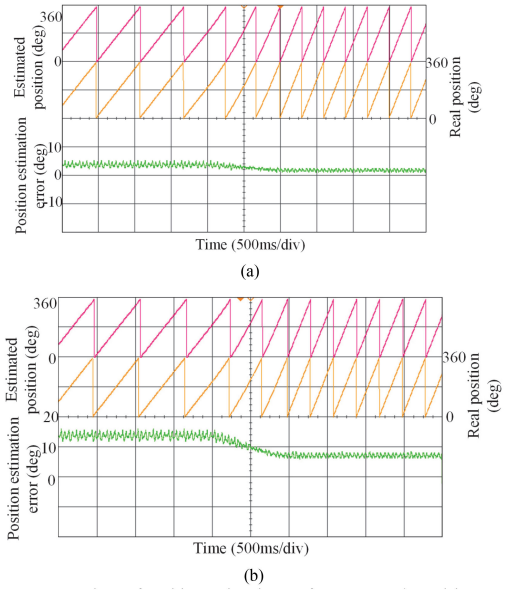

Fig. 18. Comparison of position estimation performance at slope rising speed. (a) With compensation. (b) Without compensation.

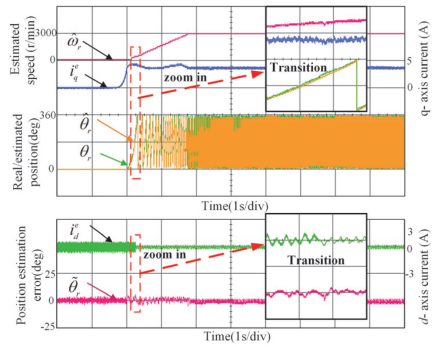

Fig. 19. Position estimation performance from start-up to full-speed based on the proposed hybrid position estimation strategy.

one voltage injection strategy. To illustrate the inverter voltage error compensation in a dynamic process, the step load between 30% and 100% rated load was further carried out in Fig. 17. Obviously, the dc offset in the position estimation error is significantly reduced after compensation in Fig. 17(a), and the position estimation error can be controlled within 7° in load transition process. Fig. 18 illustrates the waveform when the speed increases from 50 to 100 r/min with a slope. The dc offset was decreased to within 2° when the machine operated stably at 100 r/min in Fig. 18(a). Compared with Fig. 18(b) without compensation, the position error ripple also was reduced, the dynamic response and position estimation accuracy has been improved.

B. Low- to High-Speed Transition Performance of IPMSM

Note that when the initial position detection is completed and the motor starts to rotate, the value of k_n in (18) is 2. In order to evaluate the position estimation performance of sensorless drive

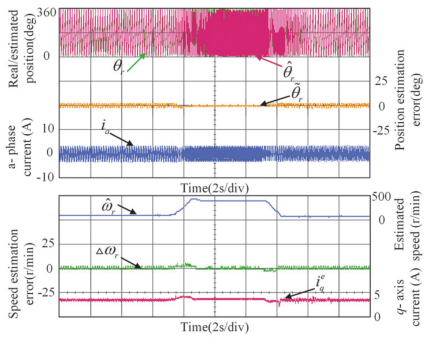

Fig. 20. Sensorless position estimation performance under the rated load during full-speed region, where the speed was changing from 100 r/min to 400 r/min, then decreasing to 100 r/min.

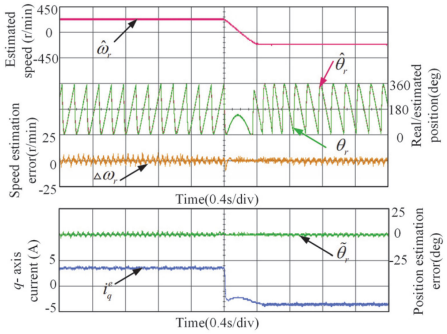

Fig. 21. Experimental results based on proposed method within the transition region under the rated load.

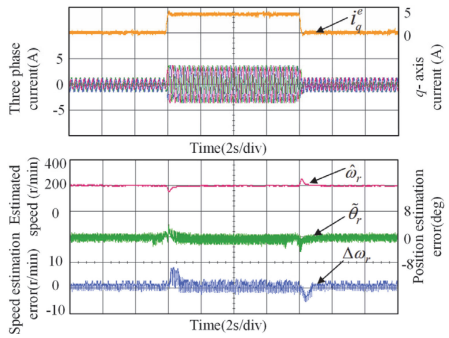

Fig. 22. Experimental results based on the proposed method within the transition region at the 100% step load and 200 r/min.

at full-speed, the experimental results are given in Figs. 19 and 20.

In Fig. 19, the estimated speed and position closed-loop in full-speed under rated load was implemented. The transition region is designed at 5% (150 r/min) and 10% (300 r/min) rated speed. The experimental results for the IPMSM startup from standstill to the rated speed of 3000 r/min were given. As can be illustrated, when the motor accelerates, i_q^e increases to overcome the load; the estimated speed can be switched smoothly from low speed to medium speed; i_d^e was decreased when the speed switched to high speed. The estimated rotor position can track swiftly the actual, and the position estimation error is less than 5.2°. From Fig. 19 with the proposed method, the sensorless drive can be steadily accelerated from zero-speed to full- speed.

Fig. 20 shows the sensorless position estimation system during the full-speed region at the acceleration and deceleration processes. The drive accelerated from 100 to 400r/min and then decelerated to 100 r/min. In the whole process, the speed estimation error is was within ± 5 r/min, and the position estimation error was less than 3.5°. From the experimental results, the proposed hybrid position observer can simultaneously satisfy the low-speed and high-speed operation, and the two-position estimation modes can be smoothly switched.

In order to evaluate the dynamic performance of the transition region. Figs. 21 and 22 show the experimental results in different situations.

Fig. 21 illustrates the sensorless position estimation system running under forward and reverse rotation state during the transition region at a speed from 225 to −225 r/min with a rated load. The corresponding maximum speed and position estimation errors were 10 r/min and 5°, respectively. According to the experimental results, the drive system can be switched stably from forward to reverse rotation.

Fig. 22 shows the experimental results during the transition region at a constant speed of 200 r/min with a 100% step load. When a step load was suddenly imposed, the estimated speed $\hat{\omega}_r$ was reduced, and then $\hat{\omega}_r$ was converged quickly to the commanded speed in a certain period. The corresponding speed and position errors were within 8 r/min and 4.8°, respectively. As a result, the drive system has good antidisturbance performance and fast dynamic response.

VI. Conclusion

In this article, the hybrid position estimation for sensorless drives was proposed of covering a full-speed. For the position estimation at zero- and low-speed, without any other testing signal injection, the HF d-axis current induced by the injection voltage itself was directly exploited for magnet polarity detection. The fast convergence of position estimation and reliability of magnet polarity detection in the MVVI method was demonstrated in experiments. Meanwhile, by injecting two opposite voltages into the estimated d-axis, the inverter voltage error was counteracted in estimating the rotor position, minimizing the inverter nonlinearity effect. The transition algorithm and disturbance compensation method were developed to switch the two methods smoothly and rapidly. According to the experiments, the transition featured good dynamic response at different speeds and torque levels, and position error during speed transients was under control. The drive system in the full-speed region based on the proposed hybrid position estimation was stable and robust.

Appendix

To ensure the stability of the designed SMO, the positive definite Lyapunov function is defined as

$$V = \frac{1}{2} S^T S = \frac{1}{2}(\tilde{i}_\alpha^2 + \tilde{i}_\beta^2). \tag{A1}$$

According to the Lyapunov stability decision theorem, if the positive definite Lyapunov function along the system trajectories, the time derivative must be negative definite, i.e., $\dot{V}<0$.

Taking the time derivative of (A1)

$$\begin{aligned}\dot{V} &= S^T\dot{S}\\ &= \underbrace{-\frac{R}{L_d}\left(\tilde{i}_\alpha^2+\tilde{i}_\beta^2\right)}_{\text{term1}}\\ &\quad \underbrace{-\frac{1}{L_d}\begin{Bmatrix}(\tilde{i}_\alpha((l\cdot\frac{\omega_c}{s+\omega_c}+1)\cdot k\cdot Z(\tilde{i}_\alpha)-e_\alpha))\\ +(\tilde{i}_\beta((l\cdot\frac{\omega_c}{s+\omega_c}+1)\cdot k\cdot Z(\tilde{i}_\beta)-e_\beta)\end{Bmatrix}}_{\text{term2}}.\end{aligned}\tag{A2}$$

Obviously, (A2) shows that term1 is always negative. Both term1 and term2 should be less than 0 to make SMO stable. The cutoff frequency of the LPF is relatively large,$\omega_c/(s+\omega_c)\approx 1$. Therefore, the observer gain can be derived to meet the following criteria:

$$(l+1)k>\max\left(\left|\frac{e_\alpha}{Z(\tilde{i}_\alpha)}\right|,\left|\frac{e_\beta}{Z(\tilde{i}_\beta)}\right|\right).\tag{A3}$$

Observed from (A3), k should be much larger because $|Z(x)|=|k\tanh(\lambda x)|$ less than 1 over the boundary layer range. In practice, $\tilde{i}_{\alpha\beta}$ are the estimation errors. They will fluctuate mainly around the sliding surface as per sliding mode theory, with little variation with the tolerance range. Definition of the lower tolerance as ξ, namely

$$\min(\left|\tilde{i}_\alpha\right|,\left|\tilde{i}_\beta\right|)=\xi.\tag{A4}$$

The minimum $Z(x)$ can be rewritten as follows:

$$\min|Z(x)|=\tanh(\lambda\xi).\tag{A5}$$

Combined with (A3) and (A5), the observer gain k can be set as

$$k>\frac{1}{(l+1)}\left(\left|\frac{e_\alpha}{\min\left|Z(\tilde{i}_\alpha)\right|}\right|,\left|\frac{e_\beta}{\min\left|Z(\tilde{i}_\beta)\right|}\right|\right)\tag{A6}$$

where l is the feedback gain of the equivalent control. When the back EMF is relatively small at low speed (5%–20% of the rated speed), $-1<l<0$, the rotor position can be calculated from the enlarged equivalent back EMF instead of the back EMF, which extends the minimum operating range of SMO, improves the position estimation performance of SMO, otherwise, $l=1$.

REFERENCES

[1] S. Sul, Y. Kwon, and Y. Lee, "Sensorless control of IPMSM for last 10 years and next 5 years," *CES Trans. Elect. Mach. Syst.*, vol. 1, no. 2, pp. 91–99, Jun. 2017.

[2] Dejan Raca, Michael C. Harke, and Robert D. Lorenz, "Robust magnet polarity estimation for initialization of PM synchronous machines with near-zero saliency," *IEEE Trans. Ind. Appl.*, vol. 44, no. 4, pp. 595–601, Apr. 2008.

[3] M. A. M. Cheema, J. E. Fletcher, M. Farshadnia, D. Xiao, and M. F. Rahman, "Combined speed and direct thrust force control of linear permanent-magnet synchronous motors with sensorless speed estimation using a sliding-mode control with integral action," *IEEE Trans. Ind. Electron.*, vol. 64, no. 5, pp. 3489–3501, May 2017.

[4] Y. Iwaji, R. Takahata, T. Suzuki, and M. Hano, "All-speed-range drive for surface permanent magnet synchronous motors by combined use of two position sensorless methods," in *Proc. IEEE 5th Int. Symp. Sensorless Control Elect. Drives*, 2014, pp. 1–6.

[5] X. Luo, Q. Tang, A. Shen, H. Shen, and J. Xu, "A combining FPE and additional test vectors hybrid strategy for IPMSM sensorless control," *IEEE Trans. Power Electron.*, vol. 33, no. 7, pp. 6104–6113, Jul. 2018.

[6] M.-Y. Wei and T.-H. Liu, "A high-performance sensorless position control system of a synchronous reluctance motor using dual current-slope estimating technique," *IEEE Trans. Ind. Electron.*, vol. 59, no. 9, pp. 3411–3426, Sep. 2012.

[7] J.Kain M.Grewal, "FPGA implementation of a hybrid sensorless control of SMPMSM in the whole speed range," *IEEE Trans. Ind. Informat.*, vol. 9, no. 3, pp. 125–1261, Mar. 2013.

[8] D. Nguyen, R. Dutta, M. F. Rahman, and J. E. Fletcher, "Performance of a sensorless controlled concentrated-wound interior permanent-magnet synchronous machine at low and zero speed," *IEEE Trans. Ind. Electron.*, vol. 63, no. 4, pp. 2016–2026, Apr. 2016.

[9] J. Lara and A. Chandra, "Performance investigation of two novel HSFSI demodulation algorithms for encoderless FOC of PMSMs intended for EV propulsion," *IEEE Trans. Ind. Electron.*, vol. 65, no. 2, pp. 1074–1083, Feb. 2018.

[10] S. Kim, J. Im, E. Song, and R. Kim, "A new rotor position estimation method of IPMSM using all-pass filter on high-frequency rotating voltage signal injection," *IEEE Trans. Ind. Electron.*, vol. 63, no. 10, pp. 5499–6509, Oct. 2016.

[11] Y. Yoon, S. Sul, S. Morimoto, and K. Ide, "High-bandwidth sensorless algorithm for AC machines based on square-wave-type voltage injection," *IEEE Trans. Ind. Appl.*, vol. 47, no. 3, pp. 1361–1370, May/Jun. 2011.

[12] R. Ni, D. Xu, F. Blaabjerg, K. Lu, G. Wang, and G. Zhang, "Square-wave voltage injection algorithm for PMSM position sensorless control with high robustness to voltage errors," *IEEE Trans. Power Electron.*, vol. 32, no. 7, pp. 5425–5437, Sep. 2017.

[13] Y. Park and S.K. Sul, "Implementation schemes to compensate for inverter nonlinearity based on trapezoidal voltage," *IEEE Trans. Ind. Appl.*, vol. 50, no. 2, pp. 1066–1073, Mar./Apr. 2014.

[14] G. Shen, W. Yao, B. Chen, K. Wang, K. Lee, and Z. Lu, "Automeasurement of the inverter output voltage delay curve to compensate for inverter nonlinearity in sensorless motor drives," *IEEE Trans. Power Electron.*, vol. 29, no. 10, pp. 5542–5553, Oct. 2014.

[15] C. Shang, M. Yang, J. Long, D. Xu, J. Zhang, and J. Zhang, "An accurate VSI nonlinearity modeling and compensation method accounting for DC-link voltage variation based on LUT," *IEEE Trans. Ind. Electron.*, to be published, doi: 10.1109/TIE.2021.3111560.

[16] S. M. Seyyedzadeh and A. Shoulaie, "Accurate modeling of the nonlinear characteristic of a voltage source inverter for better performance in near zero currents," *IEEE Trans. Ind. Electron.*, vol. 66, no. 1, pp. 71–78, Jan. 2019.

[17] G. Pellegrino, R. I. Bojoi, P. Guglielmi, and F. Cupertino, "Accurate inverter error compensation and related self-commissioning scheme in sensorless induction motor drives," *IEEE Trans. Ind. Appl.*, vol. 46, no. 5, pp. 1970–1978, Sep. 2010.

[18] L. Wang, Z. Q. Zhu, H. Bin, and L. M. Gong, "Current harmonics suppression strategy for PMSM with nonsinusoidal Back-EMF based on adaptive linear neuron method," *IEEE Trans. Ind. Electron.*, vol. 67, no. 11, pp. 9164–9173, Nov. 2020.

[19] Z. Tang and B. Akin, "Suppression of dead-time distortion through revised repetitive controller in PMSM drives," *IEEE Trans. Energy Convers.*, vol. 32, no. 3, pp. 918–930, Sep. 2017.

[20] Y. Kano and N. Matsui, "Rotor geometry design of saliency-based sensorless controlled distributed-winding IPMSM for hybrid electric vehicles," *IEEE Trans. Ind. Appl.*, vol. 54, no. 3, pp. 2336–2348, May/Jun. 2018.

[21] W. Villet, M. Kamper, P. Landsmann, and K. R., "Hybrid position sensorless vector control of a reluctance synchronous machine through the entire speed range," in *Proc. 15th Int. Power Electron. Motion Control Conf.*, 2012, pp. LS4b-1.1-1–LS4b-1.1-7.

[22] J. Liu, T. A. Nondahl, J. Dai, S. Royak, and P. B. Schmidt, "A seamless transition scheme of position sensorless control in industrial permanent magnet motor drives with output filter and transformer for oil pump applications," *IEEE Trans. Ind. Appl.*, vol. 56, no. 3, pp. 2180–2189, May/Jun. 2020.

[23] D. Vosmik, V. Smidl, and Z. Peroutka, "Hybrid estimator using advanced model selection approach for sensorless control of PMSM," in *Proc. Power Electron. Motion Control Conf.*, 2012, pp. 5–8.

[24] Z. Wang, K. Lu, and F. Blaabjerg, "A simple startup strategy based on current regulation for back-emf-based sensorless control of PMSM," *IEEE Trans. Power Electron.*, vol. 27, no. 8, pp. 3817–3825, Aug. 2012.

[25] Z. Ma, J. Gao, and R. Kennel, "FPGA implementation of a hybrid sensorless control of SMPMSM in the whole speed range," *IEEE Trans. Ind. Informat.*, vol. 9, no. 3, pp. 1253–1261, Aug. 2013.

[26] G. Wang, R. Yang, and D. Xu, "DSP-based control of sensorless IPMSM drives for wide-speed-range operation," *IEEE Trans. Ind. Electron.*, vol. 60, no. 2, pp. 720–727, Feb. 2013.
[27] Q. Tang, D. Chen, and X. He, "Integration of improved flux linkage observer and I–f starting method for wide-speed-range sensorless SPMSM drives," *IEEE Trans. Power Electron.*, vol. 35, no. 8, pp. 8374–8383, Aug. 2020.
[28] C. Zhao, M. Tanaskovic, F. Percacci, S. Mariéthoz, and P. Gnos, "Sensorless position estimation for slotless surface mounted permanent magnet synchronous motors in full speed range," *IEEE Trans. Power Electron.,* vol. 34, no. 12, pp. 11566–11579, Dec. 2019.
[29] S. C. Yang and Y. L. Hsu, "Full speed region sensorless drive of permanent-magnet machine combining saliency-based and back-emfbased drive," *IEEE Trans. Ind. Electron.*, vol. 64, no. 2, pp. 1092–1101, Feb. 2017.
[30] H. Zhang *et al.*, "A time-delay compensation method for IPMSM hybrid sensorless drives in rail transit applications," *IEEE Trans. Ind. Electron.*, vol. 66, no. 9, pp. 6715–6726, Sep. 2019.
[31] H. M. Flieh, T. Slininger, R. D. Lorenz, and E. Totoki, "Self-sensing via flux injection with rapid servo dynamics including a smooth transition to back-EMF tracking self-sensing," *IEEE Trans. Ind. Appl.*, vol. 56, no. 3, pp. 2673–2684, May/Jun. 2020.
[32] P. M. Johnson, K. Bai, and X. Ding, "Back-EMF-based sensorless control using the hijacker algorithm for full speed range of the motor drive in electrified automobile systems," *IEEE Trans. Transp. Electrific.*, vol. 1, no. 2, pp. 126–137, Aug. 2015.
[33] Z. Wu *et al.*, "Dead-time compensation based on a modified multiple complex coefficient filter for permanent magnet synchronous machine drives," *IEEE Trans. Power Electron.*, vol. 36, no. 11, pp. 12979–12989, Nov. 2021.
[34] C. Gong, Y. Hu, J. Gao, Y. Wang, and L. Yan, "An improved delay-suppressed sliding-mode observer for sensorless vector-controlled PMSM," *IEEE Trans. Ind. Electron.*, vol. 67, no. 7, pp. 5913–5923, Jul. 2020.
[35] S. Chi, Z. Zhang, and L. Xu, "Sliding-mode sensorless control of direct-drive PM synchronous motors for washing machine applications," *IEEE Trans. Ind. Appl.*, vol. 45, no. 2, pp. 582–590, Mar./Apr. 2009.
[36] R. W. Hejny and R. D. Lorenz, "Evaluating the practical low-speed limits for back-EMF tracking-based sensorless speed control using drive stiffness as a key metric," *IEEE Trans. Ind. Appl.*, vol. 47, no. 3, pp. 1337–1343, May/Jun. 2011.

Xuan Wu was born in Hunan, China, in 1983. He received the M.S. and Ph.D. degrees in automation from the College of Electrical and Information Engineering, Hunan University, Changsha, China, in 2011 and 2016, respectively.

He is currently an Associate Professor with the College of Electrical and Information Engineering, Hunan University. His research interests include permanent magnet synchronous motor drives and position sensorless control of ac motors.

Ting Wu was born in Hunan, China, in 1994. She received the B.S. degree in electrical engineering from the Hunan Institute of Engineering, Xiangtan, China, in 2016, and the M.S. degree in control engineering in 2018 from the Hunan University, Changsha, China, where she is currently working toward the Ph.D. degree with the College of Electrical and Information Engineering, Hunan University, Changsha, China.

Her current research interests include permanent magnet synchronous motor drive and position sensorless control.

Shoudao Huang (Senior Member, IEEE) received the B.E. and Ph.D. degrees in electrical engineering from the College of Electrical and Information Engineering, Hunan University, Changsha, China, in 1982 and 2003, respectively.

He is currently a Professor with the College of Electrical and Information Engineering, Hunan University. His research interests include motor drives, power electronics, and control systems.

Wenli Pan received B.S. degree in electrical engineering and automation from Northeast Normal University, Changchun, China, in 2016, and the M.S. degree in control science and engineering from the Hunan University, Changsha, China, in 2019.

She is currently a Research Engineer with Zhongxing Telecom Equipment, Wuhan, China. Her current research interests include permanent magnet synchronous motor drive and position sensorless control.

Mingcheng Lyu was born in Hunan, China, in 1990. He received the Ph.D. degree from the College of Electrical and Information Engineering, Hunan University, Changsha, China, in 2020.

Since 2020, he has been a Postdoctoral Research with the College of Electrical and Information Engineering, Hunan University, Changsha, China. His research interests include wind power generation technology, power quality control and applications of power electronics.

Yunze He (Member, IEEE) received the joint Ph.D. degree from the School of Electrical Electronic Engineering, Newcastle University, Newcastle upon Tyne, U.K., and the National University of Defense Technology, Changsha, China, in February 2012, and the College of Mechatronics Engineering and Automation, National University of Defense Technology, in December 2012.

He is currently a Professor with Hunan University, Changsha, China. In recent five years, he has chaired or participated in more than 30 projects, including NSFC and EPSRC. He has authored or coauthored more than 70 academic articles in journals and conferences, which have been cited more than 3500 times in Google scholar and the H-index is 35. He has published three books. His research interests include focused on non-destructive testing, condition monitoring, and structural health monitoring.

Dr. He is a Reviewer of more than 50 academic journals, He is selected as World's Top 2% Scientists (Career) in 2020 and 2020 Highly Cited Chinese Researchers.

Hesong Cui was born in Heilongjiang, China. He received the B.S. degree from the Harbin University of Science and Technology, Harbin, China, in 2010, and the M.S. degree from Beihang University, Beijing, China, in 2016, respectively.

He is currently a Senior Engineer with the Machinery Industry Beijing Electrotechnical Institute of Economic Research, Beijing, China. His current research interests include motor drives and power electronics.